Westfälische Wilhelms-Universität Münster
Fachbereich Physik
Institut für Kernphysik

Characteristics of a CBM Transition Radiation Detector

Marvin Fehrenbacher

WESTFÄLISCHE WILHELMS-UNIVERSITÄT MÜNSTER

Münster, September 2015
First Examiner: Prof. Dr. Johannes P. WESSELS
Second Examiner: PD Dr. Christian KLEIN-BÖSING

Abstract

Most present collision experiments in nuclear physics investigate high-energy state of matter, others like the CBM experiment at the FAIR in Darmstadt explore matter at very high densities as assumed to exist in a quark-gluon plasma.
This works aim was to provide a measurement setup and analysis procedure to gain comparable characteristics for a Transition Radiation Detector prototype as part of the CBM experiment under similar conditions.
For this, a Fe-55 photon emitting radioactive source triggered a 32-channel readout pad connected to the detectors Multi Wire Proportional Chamber.
An experimental setup with adequate gas system, high-voltage power supply, grounding and hardware readout was established and a data analysis and filter procedure was programmed to determine best parameters and important influences on data.
Hereby, it was possible to display the sources characteristic energy spectrum with an energy resolution of $(32.94 \pm 0.92)\,\%$ under these readout conditions.
Major TRD and hardware problems were detected: A sign-recognition error of the applied SPADIC readout device that prevented better trigger threshold logic and a problem in the logic structure of the TRD readout pads that complicated the procedure of merging the data of related triggered pads.
This thesis results help to compare different effects of TRD parameters and to determine the best configuration for the CBM experiment setup.

Contents

Abbreviations

AGS	**A**lternating **G**radient **S**ynchroton
ALICE	**A** **L**arge **I**on **C**ollider **E**xperiment
CBM	**C**ompressed **B**aryonic **M**atter Experiment
CERN	**C**onseil **E**uropéen pour la **R**echerche **N**ucléaire
	European Nuclear Research Center
DLM	**D**eterministic **L**atency **M**essages
FAIR	**F**acility for **A**nti-Proton and **I**on **R**esearch
FLIB	**F**irst **L**evel Event Selector **I**nterface **B**oard
FPGA	**F**ield **P**rogrammable **G**ate **A**rray
LHC	**L**arge **H**adron **C**ollider
MWPC	**M**ulti **W**ire **P**roportional **C**hamber
RHIC	**R**elativistic **H**eavy **I**on **C**ollider
SPADIC	**S**elf-trigged **P**ulse **A**mplification and **D**igitalization as **IC**
TRD	**T**ransition **R**adiation **D**etector

Chapter 1

Motivation

Physics, the 'knowledge of nature' is the scientific approach to the What the universe consist of and the How it behaves. Both questions depend on each other, because to thoroughly describe a process one needs knowledge of the participants' nature. While the behavior of macroscopic material is largely understood, there are still numerous blank spots in our knowledge of the nature and interaction of atomic and sub-atomic matter. A major goal in todays nuclear physics is to achieve this knowledge through particle collisions. With the improving technology and increasing processing power, the possibility to gain knowledge of matter via collision experiments rises continuously. While ongoing experimental programs such as the Large Hadron Collider (LHC) or the Relativistic Heavy Ion Collider (RHIC) research particle reactions at high temperatures, others such as the future Facility for Antiproton and Ion Research (FAIR) in Darmstadt seeks to investigate baryonic matter at high density as exists supposedly in neutron stars and the core of supernova explosions.

Precondition for any measurement is a thorough understanding and the optimal setup of the detector. The goal of this work was to provide an advanced characterization of, and knowledge about the parameters effects on a Transition Radiation Detector (TRD) prototype chamber as employed in the future Compressed Baryonic Matter experiment (CBM) @ FAIR.
To accomplish this, a measurement procedure under conditions similar to those in the CBM detector setup had to be developed, to gain comparable energy spectrum data of a radioactive Fe-55 photon source. Therefore, an experimental setup with gas system, high-voltage supply, grounding and a readout chain for data acquisition had to be established at best possible conditions. Furthermore, the acquired data had to be analyzed and filtered to finally allow a comparable characteristic Fe-55 energy spectrum resolution.

Chapter 2

Background

2.1 The CBM Experiment

2.1.1 Motivation

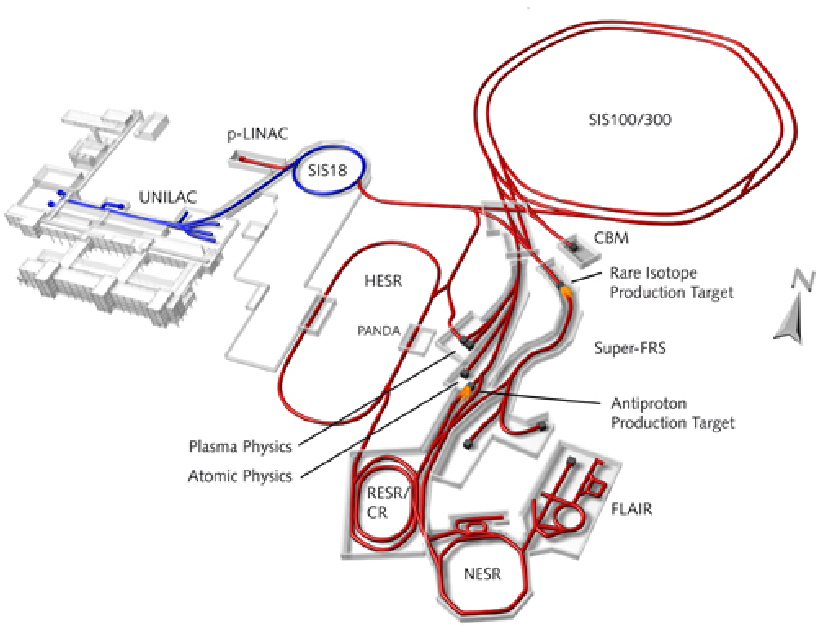

FIGURE 2.1: FAIR experiment in Darmstadt [17]

The CBM experiment is part of the FAIR in Darmstadt (see Fig. 2.1) the aim of which is to investigate highly compressed baryonic matter through relativistic heavy-ion collisions. This state of high density exists within the reaction volume of the collision which leads to the fact that varying beam energies result in varying states of density and temperature.

While most collision experiments focus on experiments at very high temperatures and

low baryon densities, the CBM experiment will allow to explore densities up to about three times that of nuclei through beam energies between 30 and 40 GeV/u. As Fig.2.2 indicates, at these beam energies and the corresponding $\sqrt{s_{NN}} = 6$ and 10 AGeV [6], highest densities are reached.
The highest yet explored energy range at high densities is 15 Gev/u at AGS in Brookhaven [2].

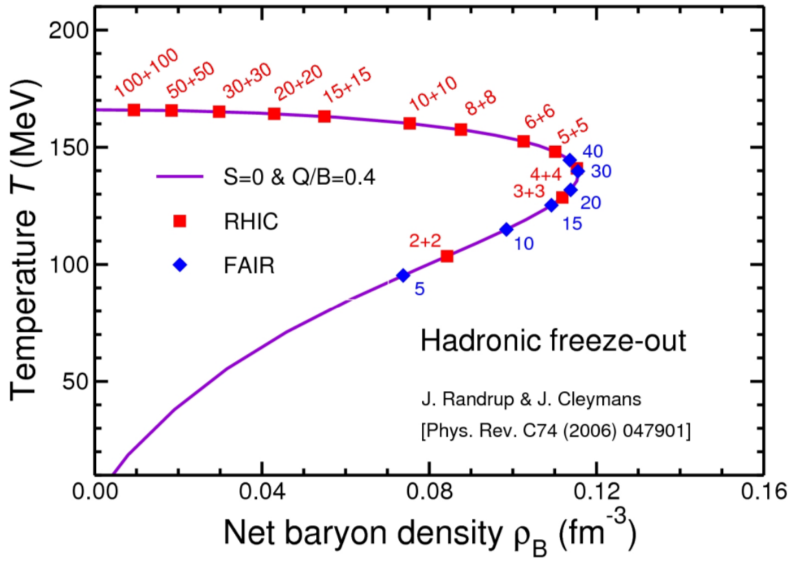

FIGURE 2.2: The hadronic critical freeze-out line formed by net baryon density and temperature of Au+Au collisions. The red values represent the total energy of each Au beam in AGeV while the blue values correspond to the kinetic force for fixed targets [18]

2.1.2 General CBM Detector Setup

The CBM experiment can be operated as a muon and an electron configuration. In the electron configuration, a Micro Vertex Detector and a Silicon Tracking System are used to track the path of primary or decay particles in less 1 m distance to the fireball at a pointing resolution much smaller than 10^{-4} m, the average decay length of e.g. D-mesons [16]. The next detector system is a Ring Imaging Cerenkov Detector to measure the velocity of charged particles to distinguish for instance pions and electrons, and various TRD layers to measure the energy loss through transition radiation and also track charged particles path. Behind the TRD, a Time-of-Flight Wall of 120 m^2 identifies hadrons. The rearmost part of the detector system consists of calorimeters to measure the energy of charged particles and neutral particles decay photons. The muon configuration especially allows momentum dependent identification to distinguish muons e.g. from J/Ψ [3].

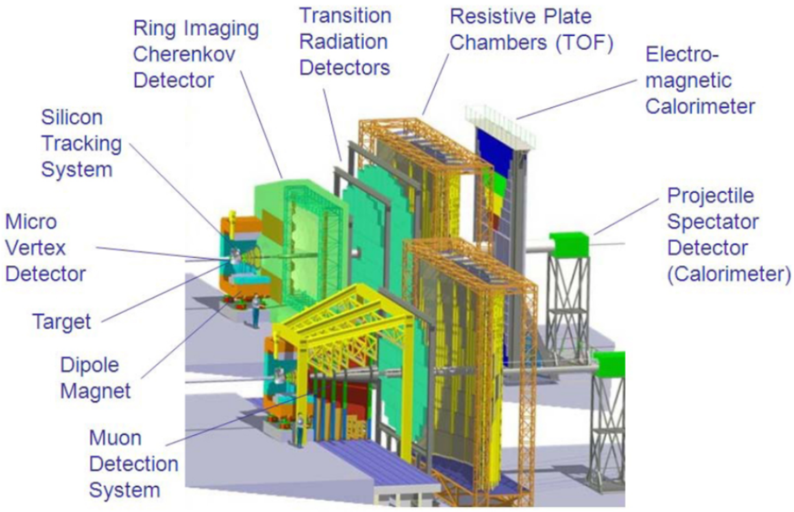

FIGURE 2.3: The two setups of the CBM experiment [13] with general setup in the back and alternative muon setup in the front

While the measured probes are the same as those in colliding experiments like the LHC, measurements at such energy-density configurations are only performed at the CBM and the RHIC in Brookhaven. This is why it is necessary to thoroughly control systematic errors through the measurement of similar collision's muon **and** electron decay branch via the different setups.
The properties of the measured decay particles yield new information about the collisions high-dense state of matter which is hypothesized to resemble the quark-gluon-plasma.

2.2 Quark-Gluon-Plasma

When with the beginning of the 20th century the study of nucleons technically evolved, indications for a partonic substructure have been found. These subparticles were called *quarks* and their strong force exchange particles *gluons*. Quarks occur for instance as constituent quarks in hadrons in patterns of three (called baryons) or two (called mesons). The quarks interaction behavior can be described by the change of their so called *color charge*. This color charge behaves in a way that the whole particle (baryon/meson) appears color neutral. If provided with enough energy, a hadronization process commences, which can be simplified as a constituent quark forming quark-antiquark-pairs and thus a single quark cannot be isolated from the parent hadron. This property is called *color confinement* and allows a study of quark behavior only at a hadron level. But it is supposed that in the quark-gluon-plasma, a state of matter of high-energy and/or density, the confinement is suspended and quarks and gluons are asymptotically free [21]. It is hypothesized that up to a few microseconds after the Big Bang the universe was in that state.

2.3 The TRD

The key to the researched matter of states properties is through the precise and fast discrimination of the collisions' decay products, e.g. positrons and pions thus defining the required properties of the TRD.
Features of the TRD are for example the high pion suppression factor to distinguish them from electrons, a precise tracking through multiple detector layers, the free streaming data acquisition and a short detector dead time [9]. Most of these features can be achieved by the comprised MWPC with suitable parameters and a radiator.

2.3.1 Multi Wire Proportional Chamber

The MWPC used in the TRD utilizes an electric field to transport electron clusters to an anode wire along its field lines and the associated ion clusters to the cathode pads, measuring the energy loss of an ionizing charged particle that traverse the chamber. The detector gas mixture normally consists of a detecting (noble) gas and a quenching gas to shorten the chambers measuring dead time. Thin anode wires are placed vertically

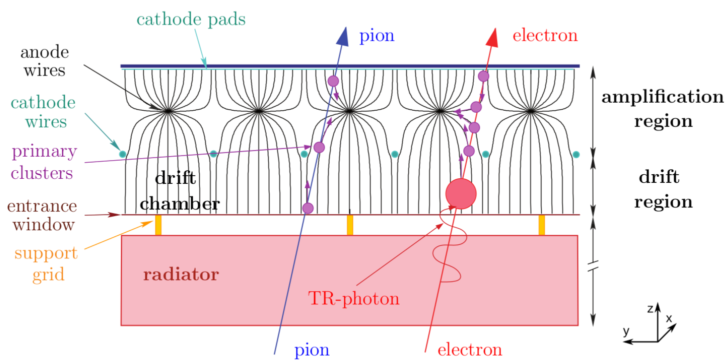

FIGURE 2.4: Schematic illustration of the TRD-MWPC [6]

in the drift chamber near a segmented plane, creating a mainly homogeneous electrical field towards the entrance window (drift region) and a stronger electrical field gradient towards the readout cathode pads of the chamber (see Fig. 2.4). If high-energy charged particles enter the drift chamber, ion-electron pairs are created through transition radiation photons' energy loss dE/dx (typically some keV/cm at normal conditions [5]). The electrons drift along the field lines towards the amplification region. If the anode voltage is high enough, avalanche multiplication occurs in the wires' near field (see Fig.

2.5). The electron avalanche is much faster than the trail of positive ions which is why they can be measured separately at the back (cathode pad plane) of the MWPC [19]. The induced charge of the ions is proportional to the traversing particles energy loss. The relatively low speed of the ion trail is the limiting factor of the TRD's measuring rate, because they shield the wires electrical field and therefore lower the gas gain [19].

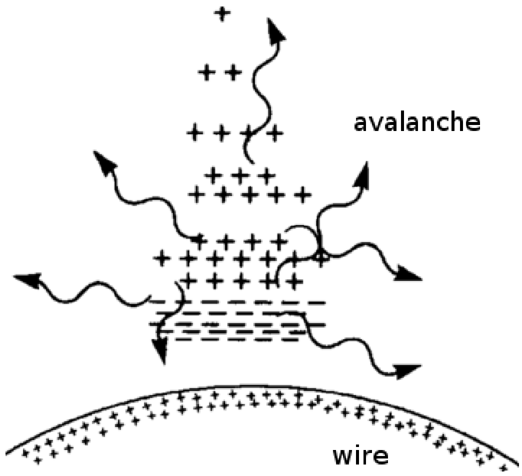

FIGURE 2.5: Schematic avalanche process at anode wires [19]

In the final setup, radiators will be established in front of the TRD. There, charged particles with a high *Lorentz factor* like electrons will emit transition radiation photons at periodic boundaries of materials with different dielectric constants. Because of their relatively high mass and therefore small *Lorentz factor* (compared to electrons of the same momentum [15]), pions don't produce transition radiation which enables the TRD's pion-suppression feature through different signal characteristics (see Fig. 2.6). The foil window must be grounded to establish the field and thin enough so that photons may still enter the active gas volume in high quantity.

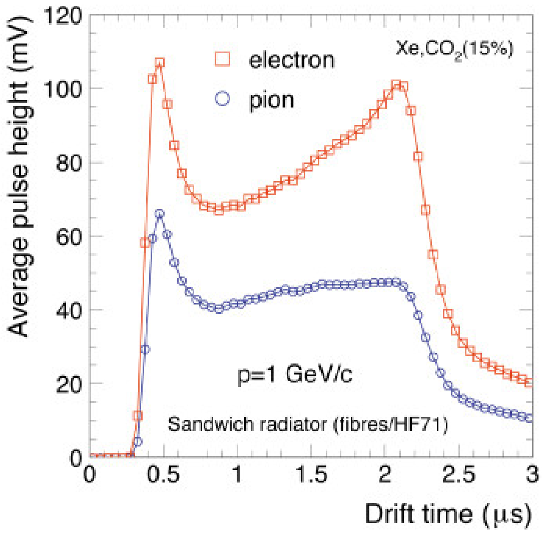

FIGURE 2.6: Average pion and electron pulse height in a ALICE TRD chamber [20]

The transition radiation photons in the final setup were simulated by a photon emitting Fe-55 radioactive source of comparable energy. The energy peak of TR-photons lies between 5-6 keV, depending on the radiators structural irregularity [6].

2.3.2 Auger Effect

The main process of primary electron cluster creation is through *Auger electrons* generated by TR photons.
An X-ray interacting with an atom (of e.g. the detecting gas) by compton- or photoeffect excites an inner shell electron. The generated vacant energy state is occupied by a electron of a higher energy level. If the energy radiated in this process excites another shell electron of a bond energy lower than the induced energy, this electron leaves the atom (auto-ionization, see Fig. 2.7) with the escape peak energy $E_{esc} = E_{Xray} - E_{bond}$. This effect is called *Auger Effect* and it competes with the effect of characteristic X-ray photon transition [22].

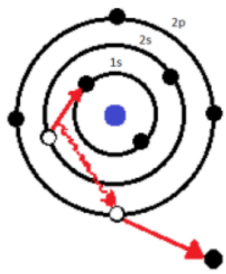

FIGURE 2.7: Auger effect [19]

Chapter 3

Experimental Setup

To provide detector conditions similar to the final setup at the CBM experiment, an experimental setup with gas and power supply as well as a Fe-55 radioactive photon source to imitate the experiment's transition radiation (TR) photons and an appropriate data acquisition had to be established.
The following section structure aligns itself to the signal processing (see Fig. 3.3).

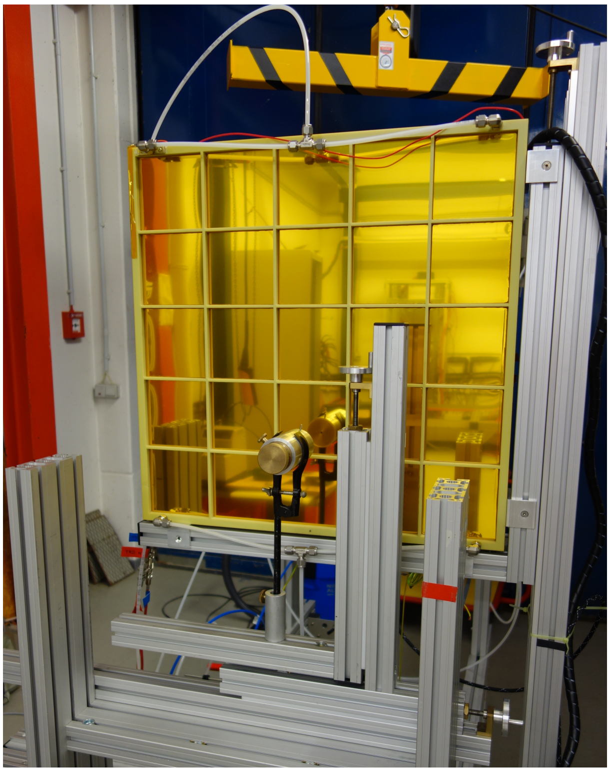

FIGURE 3.1: Foil window of the TRD setup with adjustable mounted Fe-55-source

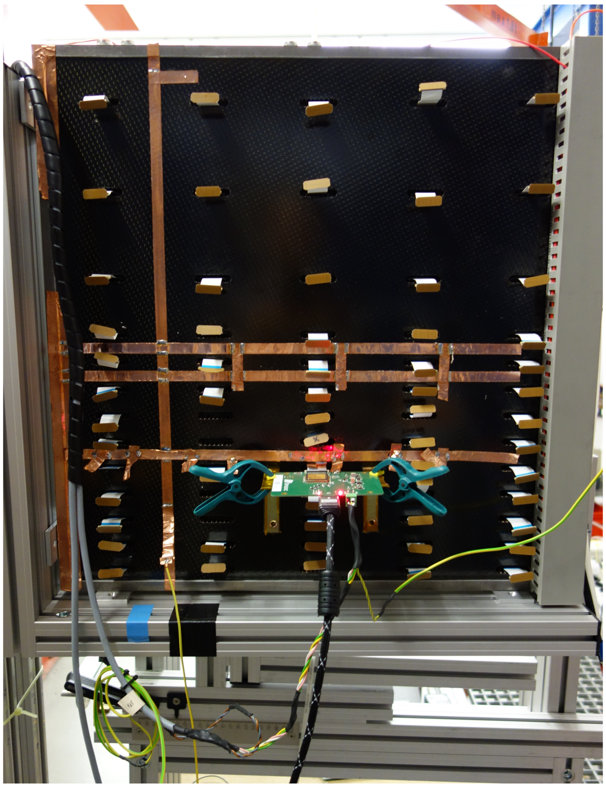

FIGURE 3.2: TRD prototype chambers backside with 32-channel-readouts and one SPADIC 1.0 attached

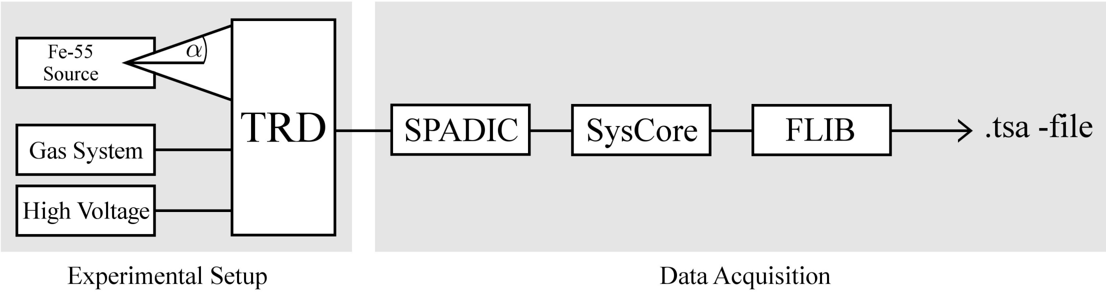

FIGURE 3.3: Schematic experimental setup

3.1 Fe-55 Source

3.1.1 General Data

The radioactive photon emitting Fe-55 sources characteristic data at measuring time can be found in Table 3.1:

TABLE 3.1: Relevant data of coin-shaped Fe-55 photon source

Radiation activity	3.63 MBq (July 2015) [A.2]
Photon output o_p	(0.51-0.82)$\times 10^5 \frac{\text{photons}}{s \cdot sr}$
Dimensions	ø 12.5 mm × 3 mm

3.1.2 Spectrum

The expected spectrum of the Fe-55 source seen by the TRD chamber has a major (weighted) peak at 5.895 keV created by the emitted photons. An additional escape peak is expected because argon may not liberate an *Auger* electron but instead a X-ray photon which can leave the chamber at an average energy loss of 2.7 keV [23].
The photons emitted by XL and XKβ will presumably not be clearly distinguishable from the noise spectrum due to their low relative probability and their broad weighted peak.

TABLE 3.2: X-ray Photon emissions of the Fe-55 source [10]

	Energy [keV]	Relative Probability [%]
XL	0.556-0.721	3.2
XKα_2	5.88765	51
XKα_1	5.89875	100
XKβ_3	6.49045	} 20.5
XKβ_5''	6.5352	

3.1.3 Absolute Photon Output

The amount of Fe-55 radiated photons that reach the TRD chamber can be approximated through the angle of beam spread α of the collimator (see Fig. 3.3). The collimator was used open so that

$$\alpha = tan^{-1}\left(\frac{d_c - d_s}{2b}\right) = tan^{-1}\left(\frac{(40 - 12.5)\,\text{mm}}{2 \cdot 5.1\,\text{mm}}\right) = (1.2156 \pm 0.0036)\,\text{rad} \tag{3.1}$$

where d_s is the diameter of the source, d_c is the diameter of the collimator attachment and b the vertical position of the source inside it each with an uncertainty of $\Delta x = 0.1\,\text{mm}$. For error calculation see Appendix A.1.
With absorption coefficient μ_{O_2} for 5.985 keV photon energy in x cm of oxygen [4] and photon output o_{ph} = (0.51-0.82)$\times 10^5 \frac{\text{photons}}{s \cdot sr}$ of the source, the rate r_{ph} of source-emitted photons reaching the TRD chamber is

$$r_{ph} = 2\pi(1 - cos(\alpha)) \cdot o_p \cdot e^{-\mu_{O_2}x} = (2.00\text{ - }3.21) \times 10^5\,\frac{\text{photons}}{\text{s}}. \tag{3.2}$$

3.2 TRD Chamber Data

The CBM-TRD used for the setup consists of a 57 x 57 cm^2 foil entrance window on one side and the readout connections for data acquisition on the other. The "active gas volume" behind the 25 μm aluminized Kapton foil is the already described MWPC with a 5 mm drift region combined with an (3.5+3.5) mm amplification section (see Fig. 3.1). There, TR-photon induced signals of the order of 200 ns are measured on (7.125 $\times$ 15) mm rectangular pads along the anode wire direction [11] (see Fig. 3.2). The Fe-55-source mounted on an adjustable frame was placed in front of different pad plane sectors to characterize the pad-planes discrepancies in the measurement of signals.

3.3 Gas System

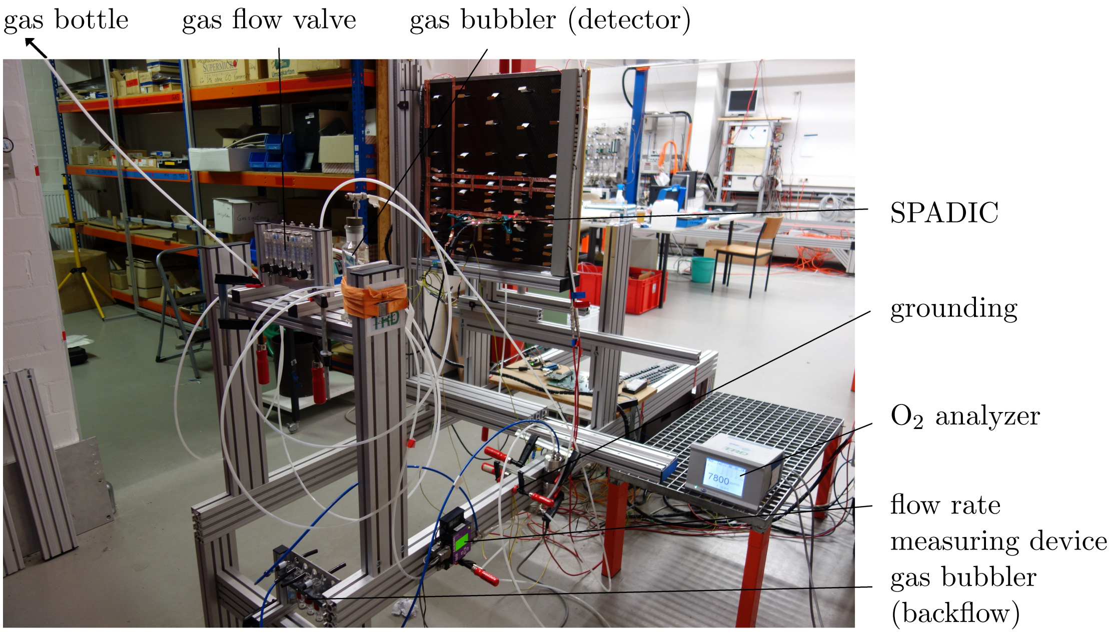

FIGURE 3.4: Gas system attached to the TRD chamber

The MWPC in this experimental setup needed a constant gas flow to create an almost clean, oxygen free active gas volume inside the chamber. For this reason, a gas system with controllable flow rate, pressure and purity had to be established (see Fig. 3.5).

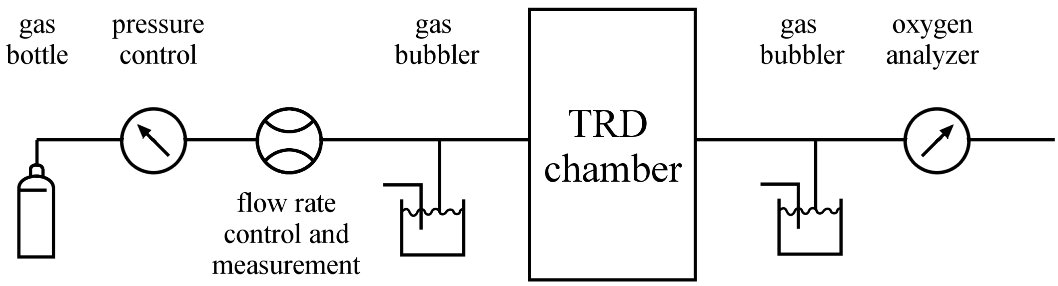

FIGURE 3.5: Schematic gas system setup

To prohibit dangerously high pressures on the kapton foil, branching pipes to gas bubblers were fit into the gas route. That prevented high initial pressures on the chamber and controlled the maximum pressure in the detector.
The oxygen percentage of the chamber gas was monitored by a *Hach Orbisphere 410* oxygen sensor as purity grade because impure gas within the MWPC could lead to lower signal efficiency because of its electronegativity at best and destructive voltage discharges because of humidity at worst. At e.g. more than 100 ppm of oxygen measured, no signal

was visible while stable measurements were possible at 40-65 ppm. Lower values were not practicable on long terms due to the permeability of chamber and gas system.
The gas used in this experiment was CO_2 as quenching gas and Argon as detecting gas.

TABLE 3.3: Gas System Settings

Gas mixture	18 % CO_2, 82 % Argon
flow rate	(2-3) l/h
pressure	< 1 bar
O_2 content	< 65 ppm

3.4 Anode and Drift Voltages

The gain factor of the MWPC could be adjusted by configuring drift and anode amplification voltage through a *ISEG EDS F025n/p* HV-power supply. All data displayed in this thesis was measured at 1750 V anode voltage respectively -500 V drift voltage if not declared otherwise.

This anode voltage provided best ADC values to match the SPADIC's dynamic energy range (app. 75 fC in 512 ADC values [1], see Fig. 3.6) as well as compromise between a high enough gain factor for the signal statistics and a too high level of noise amplification.
The drift voltage compromised between a strong electrical field to shorten the signal in time without being high enough to create too many secondary noise clusters.

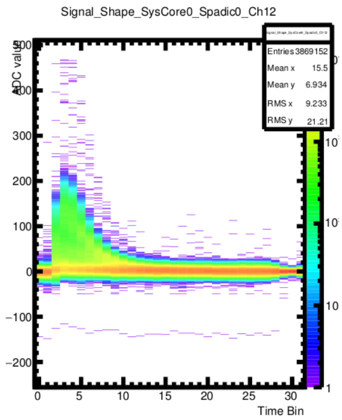

FIGURE 3.6: Signal Shape at 1750 V anode voltage and -500 V drift voltage

Like the different SPADIC's, all readout channels of the ISEG were tested for their voltage and current stability. As most stable, channel 203 (drift voltage) and channel 303 (anode voltage) were used.

3.5 Data Acquisition Hardware

3.5.1 SPADIC

The readout-device for the TRD chamber was a SPADIC 1.0.
The SPADIC is a self-triggered system for charge pulse readout (see Fig. 3.8). It was developed at the Universität Heidelberg mainly by Tim Armbruster and Michael Krieger to offer a readout system for the TRD. Each SPADIC can read out 32 channels and process them sorted by timestamps. It can be programmed for different channel triggers.

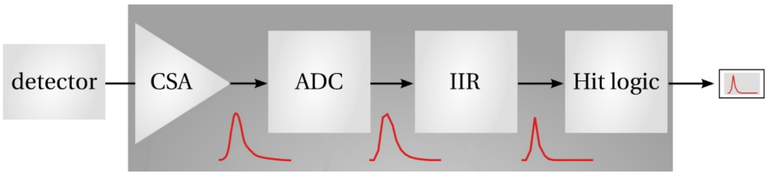

FIGURE 3.7: SPADIC schematic readout [12]

Fig. 3.7 shows the schematic structure of each Channel readout: A **C**harge **S**ensitive **A**mplifier amplifies the charge pulse and shapes it with the impulse response function $h(t) \sim t \cdot e^{-t/t_s}$ (with shaping time $t_s = 80\,\text{ns}$). Next, the signal is converted by a **A**nalog to-**D**igital **C**onverter at a resolution of 8 bits and further shaped by a **I**nfinite **I**mpuls **R**esponse filter [1].
The SPADIC's dynamic readout range reaches from -256 arbitrary ADC values to 255 around an adjustable base line. Two trigger thresholds can be set within this range to adjust the minimum ADC value at which a channel readout is triggered.

To receive best measuring results, all eleven SPADIC front-boards available were tested for their readout quality. SPADIC 05 was finally chosen as best, some others were unable to connect or had multiple broken channels.

3.5.2 SysCore

The Sys(tem)Core was developed at the Goethe Universität Frankfurt. Its primary function is the intermediation between SPADIC and **FL**ES **I**nterface **B**oard (FLIB, see below). For this, it distributes the system clock and the FLIB readout controls then builds a new container with the SPADIC's informations and a new timestamp.

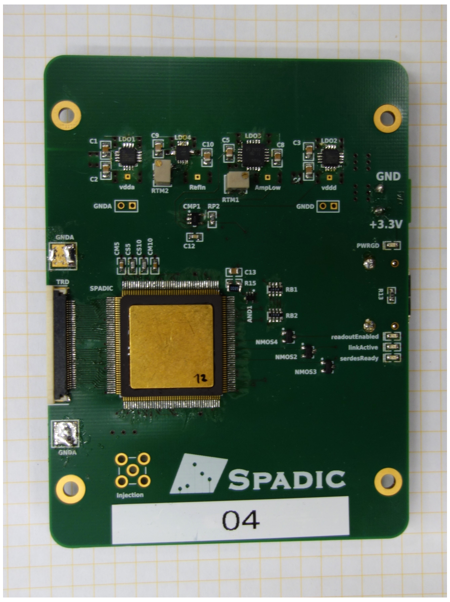

FIGURE 3.8: SPADIC 1.0 with 32-channel-connector to the left

3.5.3 FLIB

The FLES Interface Board is adjusted to a network controllable PC. FLES stands for **F**irst-**L**evel **E**vent **S**elector.
This system acquires free streaming data and combines them in timeslices instead of event-based data, further sorting them on-line and storing them in **t**ime**s**lice **a**rchive files (.tsa) [8]. The main advantage of this is the possibility to merge associated and/or overlapping events. [14]

3.6 Preparations for Measurement

In a smooth preparation for measurement one has to:

- **check the external conditions**
  High humidity may cause impurity in the chamber, significant pressure and temperature changes altered the TRD's behavior like dead time and induced charge per signal

- **install required bit-files**
  Both FLIB-PC and SysCore needed adequate firmware for a fluent communication to enable the right functional programming on these multifunctional field-programmable gate arrays (FPGAs)

- **check the links**
  Before measuring, all links between SPADIC, SysCore and FLIB-PC had to be checked and possibly reset due to full buffers

- **set the measuring parameters**
  If a fluent data acquisition was possible, a first automatic baseline setting was initialized, trigger thresholds and specialized software adjustments were set

- **start the data acquisition**
  Data was acquired by a flesnet version as long as needed and then saved in a .tsa-file

During the initialization of the data acquisition setup, software errors occurred frequently due to full buffers, unchecked external version updates and connection problems.
Buffer errors were resolved by re-enacting the last logical step and reseting SysCore and SPADIC up to restarting the FLIB-PC.
Unchecked external version updates were by far the most time-consuming errors. At best, all set parameters had to be checked/reset and the bit-files adapted. Other errors had to be fixed in individual and complex processes which will not be discussed here for its limited relevance.
Problems due to weather effect such as high humidity or pressure gradients could only be resolved by patience.

Chapter 4

Data Analysis

To receive the crucial information from readout data .tsa files, three important steps had to be taken:

1. **Clusterizing**

2. **Sorting for Displaying**

3. **Filtering and Analysing**

The program used for all analysis was CBMROOT, a specialized, C++ based derivate of the object-oriented data-analysis framework ROOT developed at CERN [7].

4.1 Clusterizing

One Fe-55 photon normally provokes an ion cluster measured on more than one channel. For this reason, a clusterizing program developed by Dr. Cyrano Bergmann was used to **merge associated messages in clusters**.
This main procedure was to sort messages by timestamp. Because primary triggers and their forcedly triggered next neighbors had identical timestamps, clusters can be recognized this way.
To distinguish different clusters with the same timestamp, clusters not adjacent in space were separated.

4.2 Sorting for Displaying

The data containers included various information about the messages such as ADC-value per timebin, SPADIC-, SysCore- and Channel-ID, timestamp and the number of all measured samples. The additional SPADIC information on signal data is given by:

- **Hit Type**
  Normal end of message: All went well (as far as stopping is concerned)
  Channel buffer full: If the single channel buffer was full during readout, message information was probably lost
  Ordering FIFO full: Same as above, but with First In - First Out readout for all channels
  Multi Hit: Channel was triggered multiple times before full message was sent
  Combinations of different Hit Types

- **Trigger Type**
  Self triggered: Channel was triggered due to set trigger thresholds
  Global triggered: All Channels were force-triggered via DLM
  Neighbor triggered: Channel was triggered by a triggered next neighbor channel
  Self and Neighbor triggered

- **Info Type**
  Information about problems during message building (timeout, corruption etc.)
  Most relevant: channel disabled during message building

All information had to be displayed in representative histograms to allow a quick overview of the measurements results and quality (see also Appendix Fig. B.1).

4.2.1 Trigger Thresholds

The first and probably most important analysis setting was to set the SPADICs trigger thresholds for signal readout. In order to measure only signals of a certain strength (the suspected signal strength) the trigger thresholds were manipulated in between the SPADIC's dynamic range of [-256; 255] arbitrary ADC values.
The SPADIC allowed two different types of trigger thresholds:

- Absolute thresholds: SPADIC triggers when two set threshold values are exceeded by two following timebins or
- Differential thresholds: SPADIC triggers when the gradient of two following timebins each exceeds the given threshold value

The final measurements were done with two equal absolute thresholds.

While two different absolute thresholds seemed to allow a better signal recognition they could not be used because (unfortunately at a very late state of the thesis) it became clear that the SPADIC had a sign-recognition error. For every measured ADC value exceeding the zero line (change of sign), this error created wrong values.
One hint to this error could be found in the decreasing high ADC values in the first timebins in Fig. 4.14 that form an unexpected signal shape.
First and second threshold are furthermore displayed as *(first ADC value)/(second ADC value)*, e.g. -170/-170.

4.2.2 Baseline

Because the original messages distribute around a largely arbitrary ADC value, each channel's signal zeroline was adjusted to the individually computed baseline.
While the former SPADIC 0.3 started the signal message 5 timebins before the triggered signal, which made it easier to find a mostly signal-unaffected baseline, the SPADIC 1.0 fixed message readout started with only one timebin prior the triggered one.
For this reason the baseline was computed through the average of the signals last timebin's ADC values. To compromise between a good average by computing enough values and a mostly signal unaffected baseline, the deviation of the noise at the end of message was observed and a baseline-signal-correlation-histogram created (see Fig.4.1-4.3).
As a signal-correlated value, the messages maximum value was chosen. It was computed through the comparison of a minimal initial value to all the messages ADC values successively and replaced if lower.

Due to overlapping readouts and triggers, some messages were cut and therefore computed bad ADC baseline values. For this reason, only full messages consisting of 32 timebins were used.

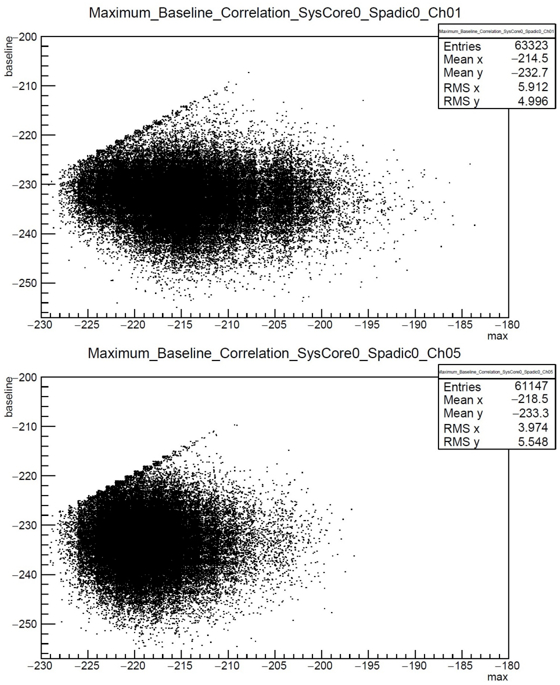

FIGURE 4.1: Maximum-baseline-correlation of different channels where the baseline is set by the messages last ADC value

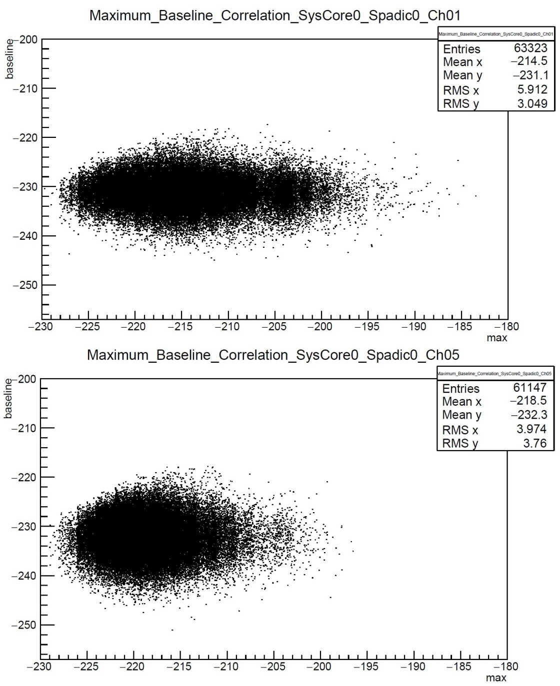

FIGURE 4.2: Maximum-baseline-correlation of different channels where the baseline is set by the messages last 3 ADC values average

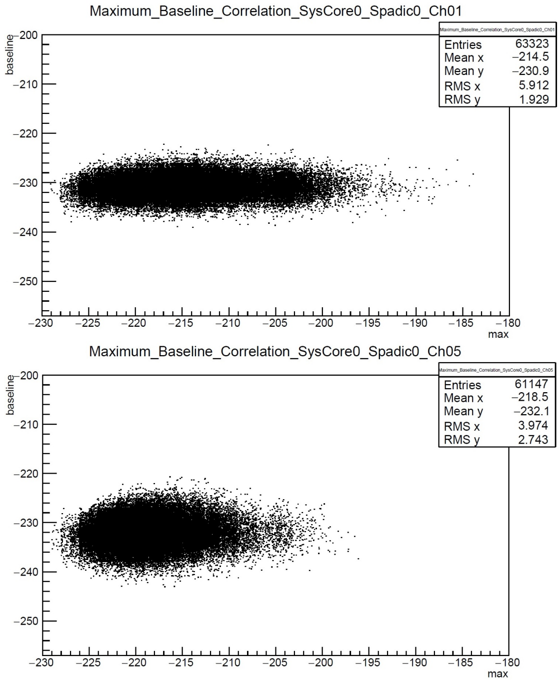

FIGURE 4.3: Maximum-baseline-correlation of different channels where the baseline is set by the messages last 5 ADC values average

If the average of more than 5 last ADC values was chosen to compute the baseline, a strong correlation with the signal height was visible in the signals shape (ADC value per 32 timebins). As best compromise for the computed baseline, the average of the last *three* ADC values was taken.

For late measurements, the SPADIC featured readout software which adjusted the channels baselines automatically could be used. This was done by forcing all channels to trigger with DLMs, and then computing the average. But the baseline program still produced visibly better signal so that it was still applied for analysis.

4.2.3 Integrated Signal ADC

To display the spectrum of the Fe-55 source, several histograms were created to display the cluster's integrated ADC values. For this, four different signal filters were chosen:

1. Only integrated maximum ADC values of cluster added (best filter, less precise statistics)
2. Only integrated ADC values greater than (baseline + 30 ADC values) added
3. Only integrated ADC values of the three timebins around the maximum added
4. All integrated ADC values from cluster added (no additional filter)

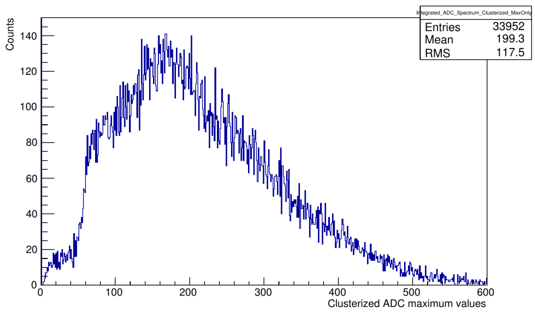

FIGURE 4.4: Only maximum integrated ADC value

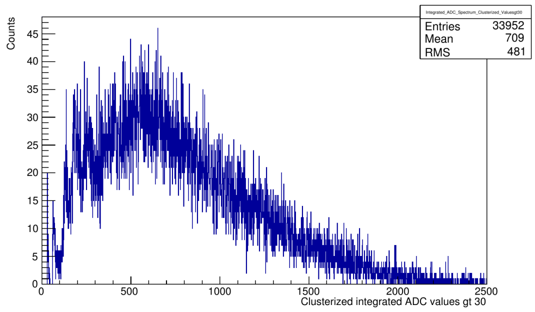

FIGURE 4.5: Only ADC values greater than 30 ADC values

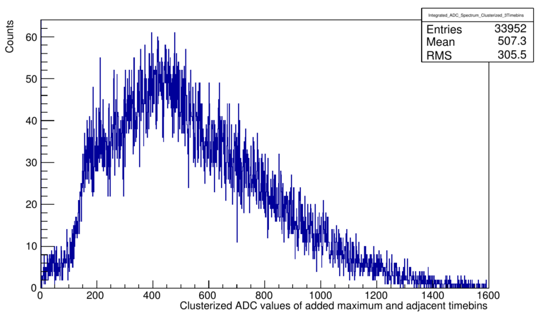

FIGURE 4.6: Only ADC values of the three timebins around maximum

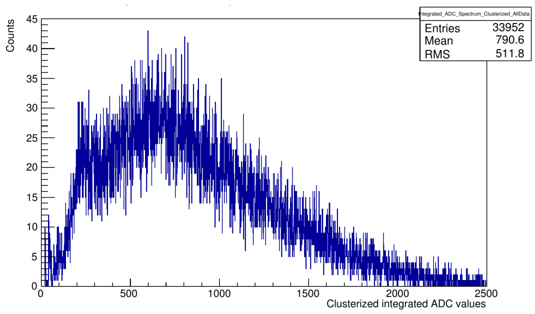

FIGURE 4.7: All integrated ADC values

Displayed is the integrated ADC spectrum of filtered maximum message values at absolute thresholds -170/-170 with the four different signal-filters. Note that the y-axis varies due to different statistics.

4.2.4 Signal Shape

Each channel's measured ADC values were plotted against the 32 timebins forming the Signal Shape. This formed one of the first and best histograms to identify good measuring and setup structure. Put simply, the comparison between the displayed signal shape (see Fig. 4.9) and the one expected due to previous measurements with a TRD prototype by Martin Kohn at CERN 2014 provided important clues to problems in the measuring setup.
Additional information could be gathered by the different signal and noise behavior among the channels (e.g. for altered grounding).

4.2.5 Clustersize per Integrated Spectrum

Because the size of the clusters had a major influence on the integrated ADC value, it was important to verify a reasonable distribution of clustersizes per integrated ADC value (see Fig. 4.8). This means that most clusters should consist of the ADC values of *three* triggered pads, and the amount of clusters of more pads should exponentially decrease in number. Ion clusters of higher charge normally provoke signals on *more than three* pads, therefore the content of bigger clustersizes should increase with higher ADC values and most outer channel clusters (*two* pads triggered) should be found at lower values (first interval).

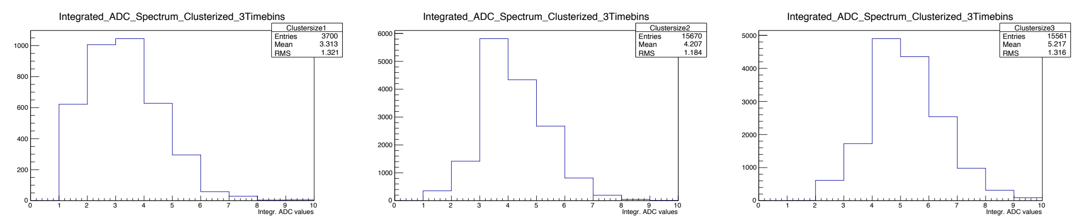

FIGURE 4.8: Clustersizes of a measurement at absolute thresholds -170/-170 for first noise interval (left) main signal and escape peak interval (middle) and higher values interval (right)

These histograms intervals were set at [0;50], [50;200] and [200;∞) ADC values.

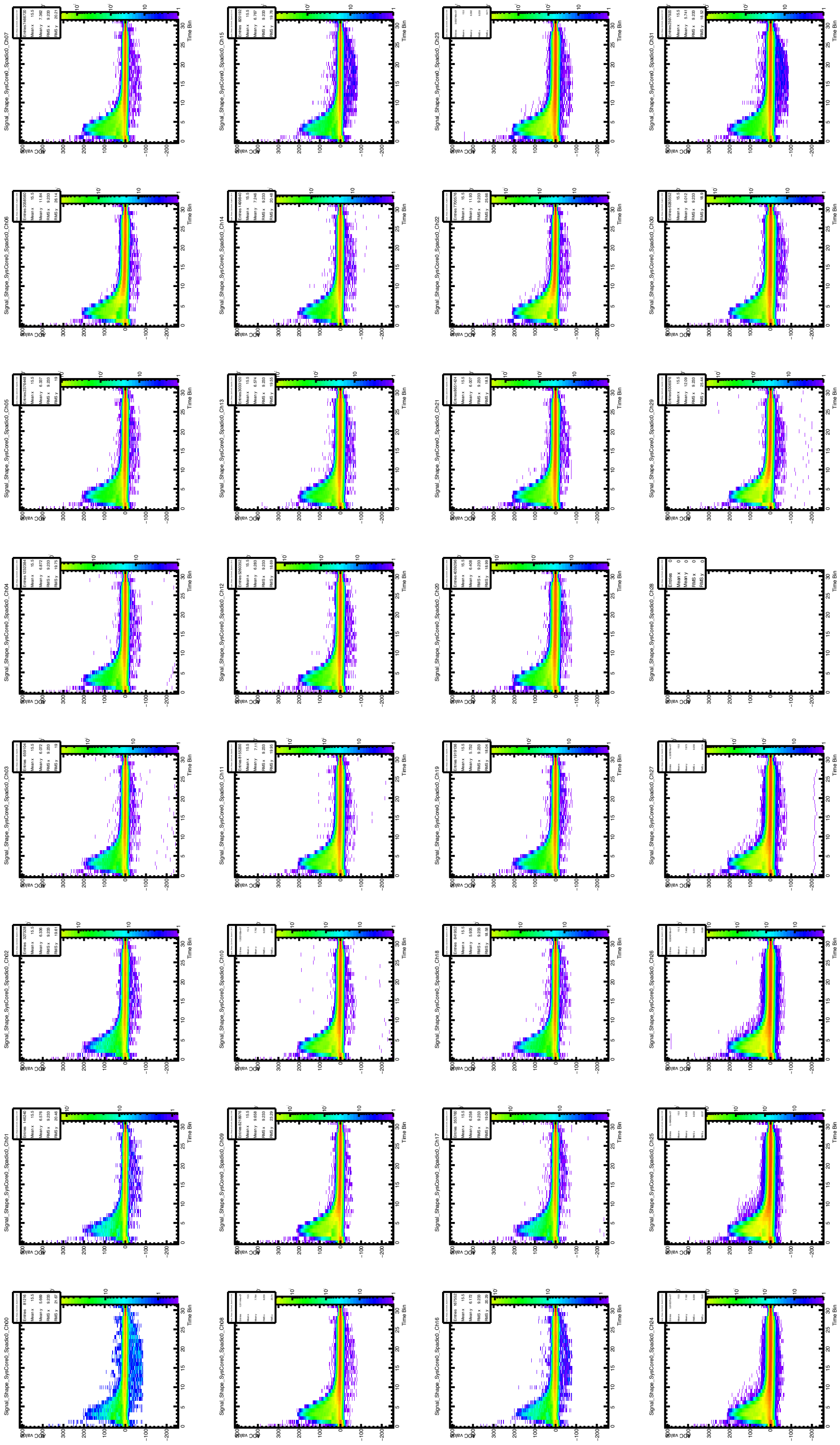

FIGURE 4.9: Signal Shape of all 32 channels measured at absolute thresholds -170/-170 and disabled Channel 28

4.2.6 Signal to Noise Ratio

To gain a fast first information about the measurement settings quality, a counter was set into the analysis program with the following formula:

$$\text{signal/noise ratio} = \frac{\text{number of messages with max. amplitude} \;>\; \text{max. noise value}}{\text{number of all messages read out}}$$

This allowed only a rough discrimination because some signal peaks were lower than the maximum noise peak. Late measurements were at noise ratios of about 30 %.
Additionally, a histogram monitoring the triggered signals shape in real-time showed that the connection to channel 28 of the SPADIC was broken which seemed to cause the adjacent channels to trigger continuously. This lead to a very bad signal/noise proportion. When channel 28 readout was disabled (see Fig. 4.9), data improved significantly.

4.3 Filtering and Analysing

Technical and software problems as well as disruptive physical effects like cosmic radiation pollute the shape of the measured signal. Their causes had to be recognized to improve measuring parameters and setup and to program filters which distinguish noise effects from signal data. It was therefore necessary to:

- Consult Stop, Trigger and Info Types whose information allowed to **check the measurements validity**
- Compare the trigger count of all channels to **detect readout problems**
- Program various filters to **reduce the signal/noise ratio** in final histograms
- Consult the Signal Shape of each channel and the cluster size distribution to **detect noise effects and acquisition problems**
- Program **problem-related analysis counters and histograms** for e.g. cluster-structure, signal amplitudes or noise-rate per channel

4.3.1 Grounding

Fluctuations or differences of the setup voltages zero line had major influences on the data accuracy. Therefore, a reasonable grounding was a necessity for any measurement. For instance, the grounding influences the measured signals noise. The outer channels of the pad mainly measured sinusoidal noise which appears to happen in the internal SPADIC electronics when the channel is rarely triggered (this was verified by placing the source vis-á-vis the pads rim which shifted the sinusoidal noise to inner channels). The noises sine frequency of approximately 3.5 MHz changed to higher frequencies (see Fig. 4.11 and 4.12) when an advanced grounding was applied. These groundings can be found in Fig. 4.10. Signal Shapes with a direct SPADIC grounding can be found in the Appendix (see Fig. B.3).

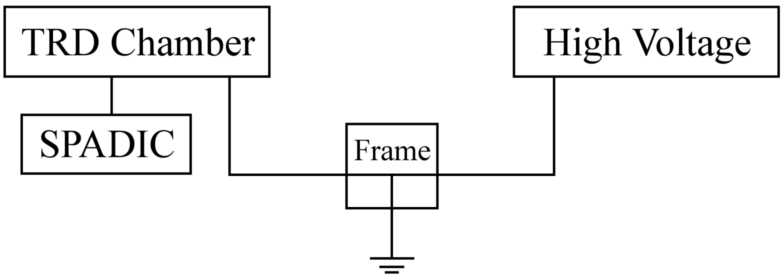

FIGURE 4.10: Final experimental setup grounding

All wire connections were soldered or tinned and fixed to the frame. It can be observed that especially the noise in the outer channels seemed to be triggered by a signal due to its maximum amplitude in the middle of the message.

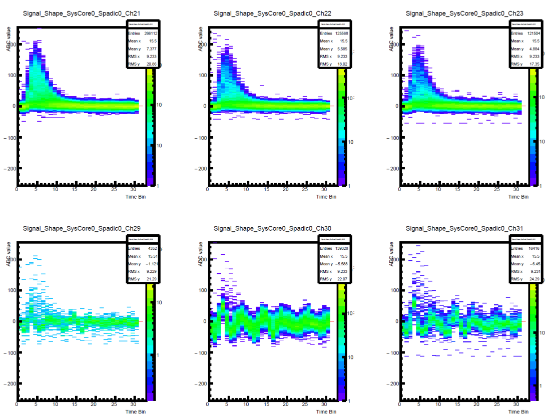

FIGURE 4.11: Signal shape of inner (up) and outer (below) channels with first grounding

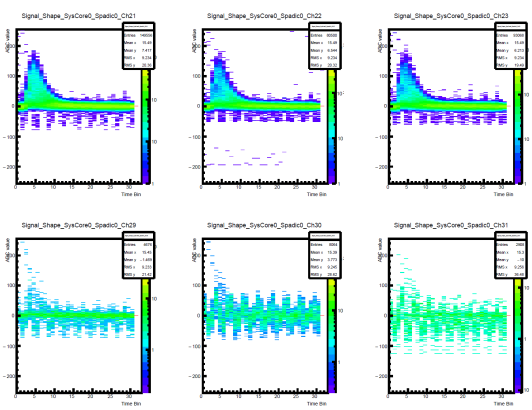

FIGURE 4.12: Signal shape of inner (up) and outer (below) channels with advanced grounding

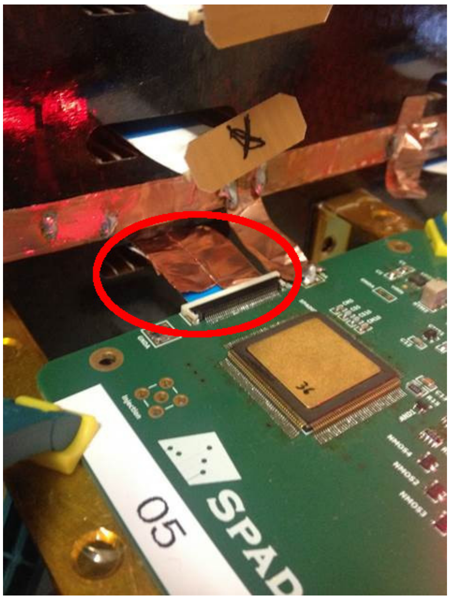

FIGURE 4.13: Copper tape shielding at SPADIC readout channel

Because of the grounding effects on the sinusoidal noise it was likely to derive from a capacity self-reinforcement in the readout cables. To alter this capacity, copper tape was adjusted on the readout cables between SPADIC and pad which reduced the sinusoidal noise (see Fig. 4.13 - 4.15).

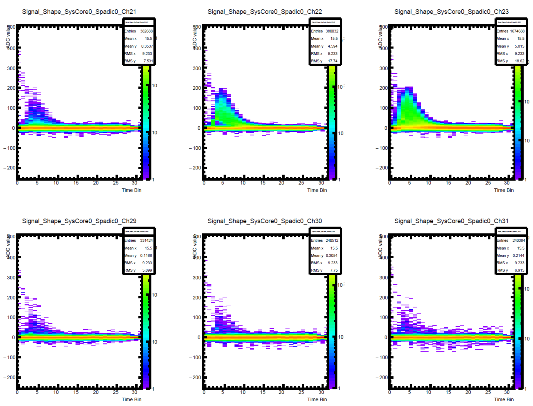

FIGURE 4.14: Signal shape of inner (up) and outer (below) channels without copper tape

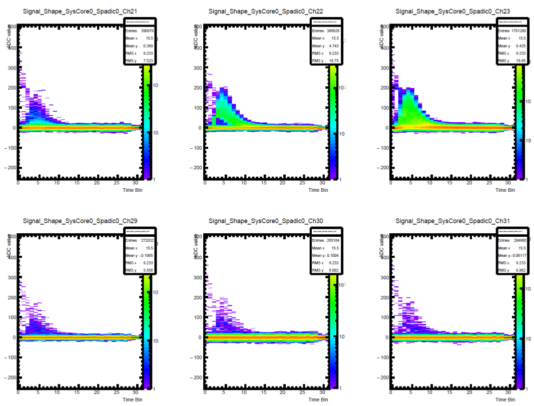

FIGURE 4.15: Signal shape of inner (up) and outer (below) channels with copper tape

4.3.2 Noise Filters

The following adjustments were used to filter noise from signal data for final histograms:

- **Compute only Normal End of Message**
  This means that neither Multi hits nor messages with full FIFO or other buffers were computed for the final spectrum

- **Filter single message clusters**
  Each triggered signal induced the readout of its adjacent channels through Forced Neighbor Trigger to get more information of the triggering signals charge and position. Therefore the minimum number of channels per cluster is three in the center and 2 for the outer channels. Possible clusterizing program and readout bugs could be filtered when only messages of clustersizes greater than one were read out.

- **Amplitude relation filter**
  The message was split into two halves and the maximum ADC value of each was computed. This lead to the following maximum relation:

  $$\text{maximum relation} = \frac{\text{maximum ADC amplitude (messages first half)}}{\text{maximum ADC amplitude (messages second half)}}$$

  Because due to the trigger logic the signal was always found in the messages first half (e.g. see Fig. 4.11 - 4.15) a low maximum relation indicated a signal-free message. This relation could only work so well due to the altered grounding and shielding.

- **read out only full messages**
  Messages of a length less than 32 timebins included unpredictable signal information and may therefore cause unpredictable signal spectrum pollution.

4.4 Clusterizer Update

A problem of the clusterizing tool caused a significant misunderstanding of the resulting spectrum: The Gaussian-shaped second peak (see Fig. 4.16 left histogram, red fitted peak) was mistaken for the signals spectrum (first peak).
This lead to many fruitless attempts to alter the bad energy resolution of this peak and later the search for its origin in program data.
Amongst other things, the extraordinary magnitude of cluster sizes (mainly consisting of 6,7 or 8 triggered channels) in this part of the spectrum (see **4.2.5**) lead to the conclusion that a clusterizing tool error could be the cause.

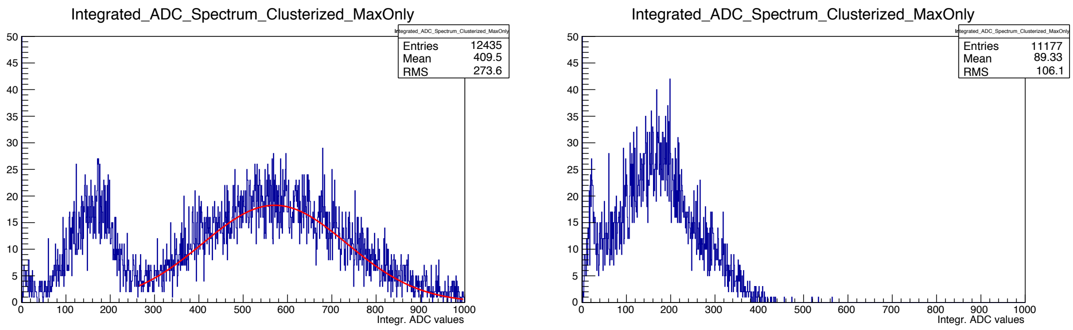

FIGURE 4.16: Integrated ADC spectrum of filtered maximum message values at differential thresholds 30/-30 before (left) and after clusterizer update (right)

When a new recognition tool was added to the clusterizer to **distinguish between multiple adjacent small clusters and real clusters measured on multiple channels**, the peak disappeared and added to the statistics of the real signal peak (see. Fig. 4.16).
This recognition tool was able to distinguish most clusters adjacent in space by two new filters. Clusters were separated by
1. Trigger Type:
If two forced neighbor triggered channels were adjacent in space, the clusters were separated. If a forced neighbor channel was bordered in space by two primary triggered channels its message was sorted into both clusters.
2. Gradient:
If a triggered channels integrated ADC value was higher than its neighbors antecedent in space, the cluster was split into two at that channel. This was recognized by a change of the derivatives sign.

Chapter 5

Results

The simplest way to compare the analyzed TRD chamber's characteristics with other designs of the detector is to measure the resolution of the Fe-55 signal peak. The intended aim of the experimental and programming procedure was to provide an energy spectrum that could discriminate escape peak from both noise and main signal peak as well as an energy solution as good as possible.

The other major part of the results were the important parameters (e.g. trigger thresholds) and analysis procedures used, and other important influences on the detectors measuring quality (e.g. grounding) recognized.

To allow a concise overview, the effect of the most important steps to improve the integrated ADC-spectrum are displayed.

5.1 Final Settings

Best measurements were provided by the following parameter setting:
(see Appendix Fig. B.2)

TABLE 5.1: Final Parameters for Experimental Setup

Anode Voltage	1750 V
Drift Voltage	500 V
Trigger Thresholds	-170/-170 ADC values (absolute)

5.2 Signal Spectrum

When data acquisition was finally working, a first histogram was generated by simply adding all messages integrated ADC values (see Fig. 5.1). A rough first filter cut lower ADC values (< 25 ADC values) due to their probable noise origin. This was the starting point for analysis development.

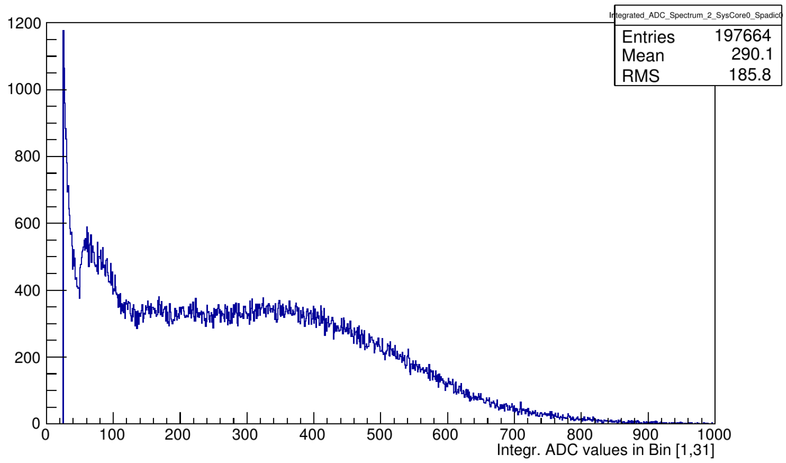

FIGURE 5.1: First unclusterized signal spectrum

The updated **clusterizing tool** and **advanced measuring parameters** led to first signal spectrum characteristics with lowered event counts per value because of the clusterized messages (see Fig. 5.2).

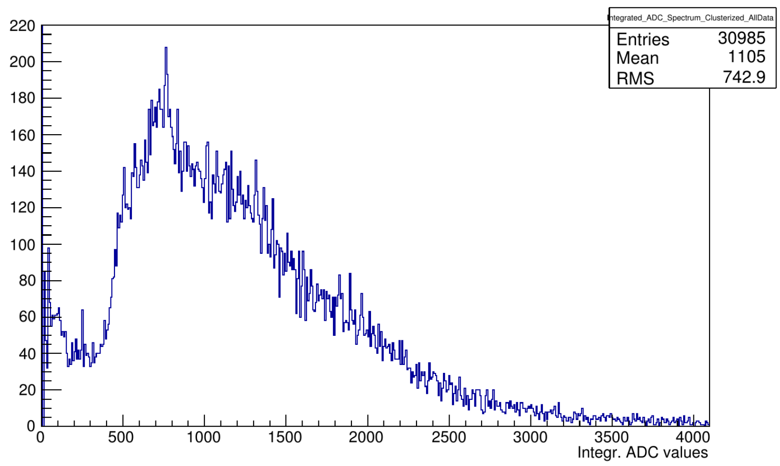

FIGURE 5.2: Clusterized signal Spectrum with two different absolute thresholds at -250/-120

Advanced grounding reduced the noise ratio. When the trigger threshold were **set at the same value** to reduce the effect of the SPADIC 1.0's sign-recognition problem (see Fig. 5.2), the signal spectrum shape for higher values improved significantly (see Fig. 5.3). The former signal peak displays a visible cut in statistics which is probably caused by the wrongly computed events exceeding the zero line at the second timebin, which corresponds to the second trigger threshold.
The following three histogram's data is binned to allow a better overview. The final histogram without binning can be found in Appendix Fig. B.5.

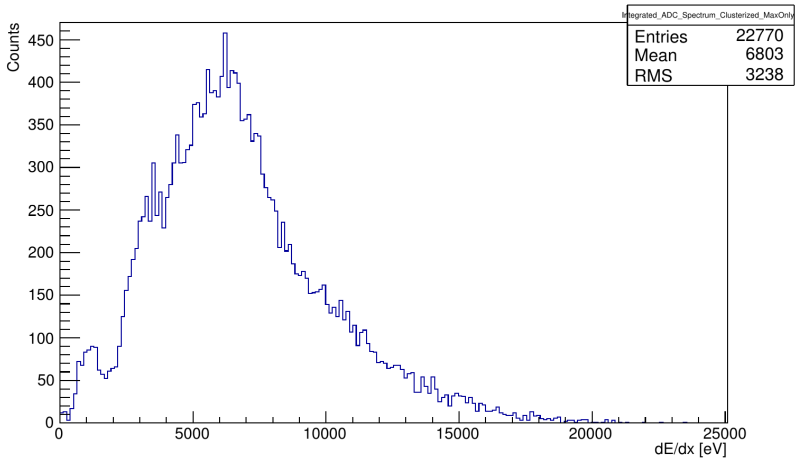

FIGURE 5.3: Integrated maximum values of measurement at final parameters

The final histogram with applied **filters** can be found in Fig. 5.4. Noise is visibly reduced at low values and the signal peaks gauss shape pronounced.

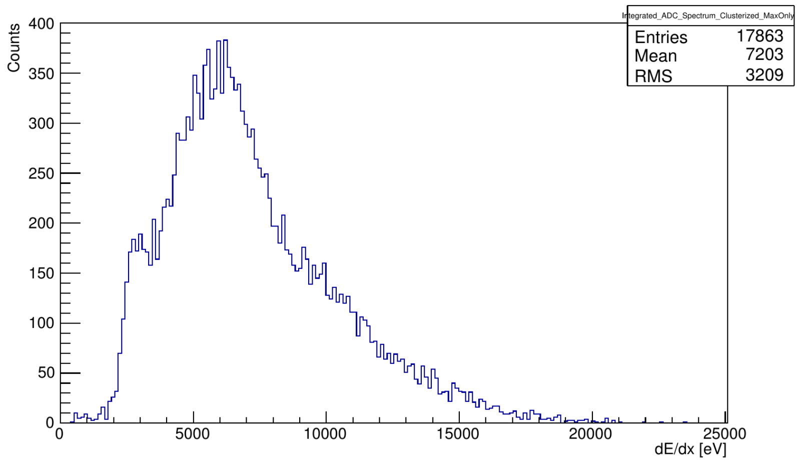

FIGURE 5.4: Final filtered Integrated ADC spectrum measured at absolute thresholds -170/-170

5.2.1 Final Spectrum with Energy Resolution

For the final signal spectrum histogram, only maximum values were computed. The energy resolution was best at this option but still comparable to the others.

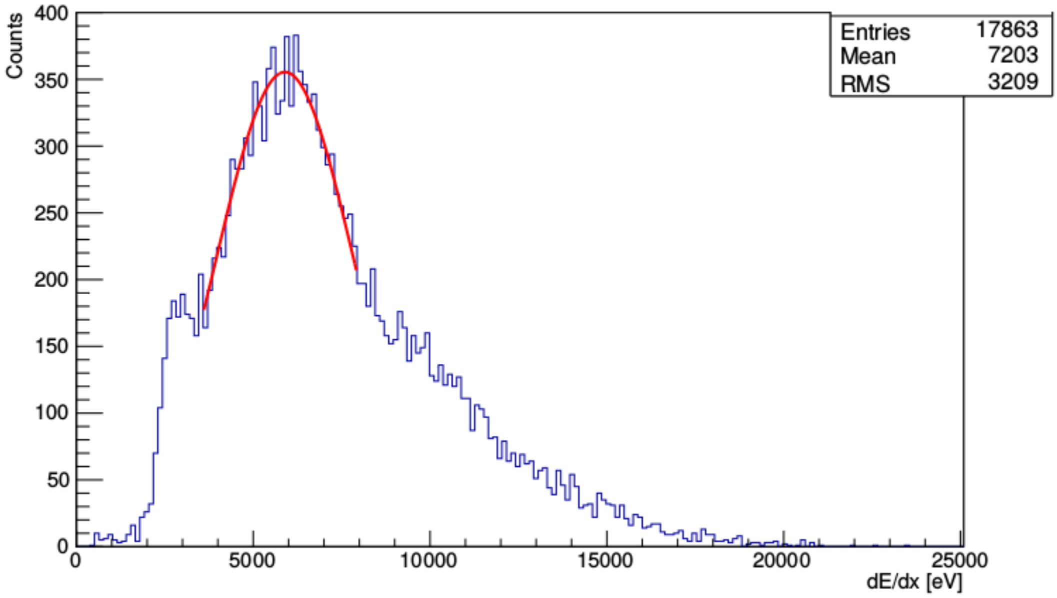

FIGURE 5.5: Final filtered Integrated ADC spectrum measured at absolute thresholds -170/-170 with applied Gaussian fit-function (5.2) and 35 min measuring time

The energy resolution (variance) of the Gaussian fitted with CBMROOT was **(32.94 ± 0.92) %**. The data were converted from ADC values to eV through the identification of the two peaks positions with the weighted main peak at 5.985 keV and the escape peak at 2.7 keV [10] through a best-fit line of gradient m and offset b (measured data cannot be arbitrarily low):

$$m \cdot (\text{ADC value}) + b = 34.413\,\text{eV} \cdot (\text{ADC value}) + 325.108\,\text{eV}$$

The fits equation is:

$$f(E) = A_{K\beta} \cdot \exp\left(\frac{E - E_{K\beta}}{\sigma_{K_\beta}}\right)^2 \tag{5.1}$$

$$= 355.50 \cdot \exp\left(\frac{E - 5985\,\text{eV}}{1941.61\,\text{eV}}\right)^2 \tag{5.2}$$

Uncertainties can be found in the Appendix A.1.

A second fit was made for the final spectrum with two additional gauss peaks at 6.49045 keV (Kβ_5'' peak) and 6.5352 keV (Kβ_3 peak) and a combined amplitude of $\frac{41}{302}$ times the major peaks amplitude, for an even more realistic fit function (see Fig. B.4). This was not used as final result, because the weighted position and low amplitude of the two Kβ peaks held too many uncertainties for a comparable energy resolution fit function. This fits equation with set energy resolution of 32.63 % is:

$$f(E) = A_1 \cdot e^{\left(\frac{E-E_{K\beta}}{\sigma_{K\beta}}\right)^2} + \frac{41}{302} \cdot A_1 \cdot e^{\left(\frac{E-E_2}{\sigma_2}\right)^2} \tag{5.3}$$

$$= 314.77 \cdot e^{\left(\frac{E-5985\,\mathrm{eV}}{1941.61\,\mathrm{eV}}\right)^2} + 43.44 \cdot e^{\left(\frac{E-6490.45\,\mathrm{eV}}{2137.95\,\mathrm{eV}}\right)^2} \tag{5.4}$$

A fit for all integrated clusterized data with the same settings computed an energy resolution of (33.98 ± 1.36) %.

Chapter 6

Discussion and Conclusion

6.1 Final Spectrum

The major goal for an advanced comparable setup is reached by a displayable energy spectrum of the Fe-55 source that allows a discrimination of the escape peak from the main signal's peak.
The observed peak was verified to be the escape peak due to its nearly unchanging relative height and position at different settings and adequate filtering methods to distinguish it from noise peaks.

Cosmic and background radiation are presumed reasons for the exponential decreasing count number at high values. These could not be influenced by applied noise filters without shielding and are therefore induced signals. Another part may originate from avalanche amplification creation near cathode wires which would create strong noise signals. Possible radiation from the aluminum collimator was measured prior to measurements and can be neglected.

The energy resolution of $(32.94 \pm 0.92)\,\%$ is not good enough for a final setup as a detector. The major reason for this is likely to be the trigger threshold problem.
Other strong influences on the measuring quality not directly related to the chamber were recognized and described.
If a realistic fit function with the weighted Kβ-peak would have been possible, the resulting energy resolution would probably have been slightly better.

6.2 Thresholds

The most influential yet unfortunately buggy measuring parameter were the trigger thresholds.
The sign-recognition problem frustrated the obvious attempt to use two suitable different thresholds per one timebin, and so only equal leveled or differential filters could be used. The problem is obvious: A rough filter two timebins wide provided very bad statistics by applying only for very few signal messages.
Triggering with differential thresholds produced other problems: The strong sinusoidal noise effects in the outer channels would cause too many triggered noise messages.

6.3 Fe-55 Sources Activity

Due to the source's radioactive half-life of 2.737 years [10], its activity was much lower than in the only somewhat comparable measurements with a SPADIC 0.3. For this reason, the collimator was used opened to improve the rate of photons reaching the detector.
The Fe-55s effective activity of (200-321) kHz during measurements compared to the proposed final event rate of 107 kHz (100 kHz/cm$^2\times$ pad-surface [5]) was of a similar but higher level. An activity in this order will lead to less multiple hits and less interaction with the space charge of previous signals which can have a positive influence on the energy resolution and the data's validity. Under these circumstances, the computable chance for a multi hit is $P(\text{multi hit}) = 7.52{\cdot}10^{-5}$ (see Appendix eq. A.4) with the additional chance of a Force Neighbor Triggered multiple hit.

6.4 Clustersize per Integrated ADC Value Histograms

The histograms (see Fig. 4.8) indicate several problems:
1. Some clusters include only one channel's values. Every primary triggered channel triggers a readout of its neighbors so that the minimum number of channels per cluster should be two for the edge channels. This means that each of these one-pad clusters was corrupted due to e.g. buffer overflow, incomplete messages or timing bugs.
2. The clusterized data of the edge channels (mainly clusters of size 2) displays only partial information about the events charge. Therefore, edge channel clusters contain only partial information of the induced charge. This may be prevented in the final chamber setup by linking border clusters when the outer channels are triggered.
Another problem was the structure of the readout channels. The pad is divided into

four logical rectangles so that in the middle, adjacent channels were not recognized as neighbors. If the source would be placed opposite to the middle of one of these rectangles, more full clusters would have been measured, but it was necessary to display this effect as long as the pad logic is not modified.

3. The main part of clusters is expected to be of size 3, exponentially decreasing. High integrated ADC-values show a different trend which may be caused by the (noise) avalanches evolving at the cathode wires due to the high electrical field or background and cosmic radiation effects.

6.5 Filters

The filtering effect is visible in Fig. 5.4 and the filters are obviously able to distinguish noise from signal data. Due to the very good applied parameters, the effect is not too strong. On beam time data or measurements with worse parameters the filters are significantly more effective.

6.6 Clusterizer

The clusterizing tool is an important part of the analysis procedure as can be seen in Fig. 4.16. It is difficult if not impossible to ideally separate clusters with this readout system. The clusterizing update was a major step in this direction but it still contains several problems:

Firstly, because the ADC values of a channel bordered by two primary triggered channels are added to both clusters, they compute too high values. This could possibly be improved by adding only half values to both clusters.

Secondly, the gradient filter would detect a possible noise peak in one cluster as a separation condition. This problem could be diminished by a clean surrounding and shielding.

6.7 Research Approach

Because the main measuring parameters strongly interfered with others, it was not possible to set them one by one.

It was therefore necessary to repeat most measuring series when a major problem's origin was understood and the problem resolved, and also when a major best parameter (like e.g. trigger thresholds) was set.

Additionally, the effect of weather situation (air humidity and pressure) or room ventilation had to be considered, because it visibly influenced data at extreme conditions.

6.8 Outlook and Conclusion

The most important result of this work was a readout procedure established from scratch. It was the first time a laboratory readout with these components was made possible and a huge amount of time was spent to take the numerous steps on this way.

This thesis results can be (and are) employed in numerous ways:

- **Comparison to other detector designs**
  The Münster TRD chambers characteristics can be compared to e.g. the TRD prototype of Frankfurt's CBM work group to characterize the influence of different chamber parameters like pad height or wire spacing on measuring quality. Also, the effect of the pad's subdivision into four rectangles on the clusterizing ability raises the subject of modified pad link-up for all TRDs
- **Data analysis**
  The effective signal filters employed can be used for TRD data analysis of laboratory and beam time data. Especially the amplitude relation filter allows a very effective noise filtering for all TRD data
- **SPADIC 1.1 development**
  The SPADIC 1.0 readout problems provide important information for the ongoing development of the next SPADIC generation
- **Experimental setup**
  The final setup of grounding, data acquisition and voltages can be used for similar testing setups or even utilization in the final detector setup

Further possible investigations are:

- Measurements comparing different readout pads
- Another adjustment of the voltage comparison
- A repetition of measurements at similar parameters with the new SPADIC 1.1

Different Pads Measurement

To further characterize the TRD, the differences in e.g. energy solution and signal reception quality of pads in different sizes and position to the source can be investigated to gain information of the chambers border effects.

Anode High Voltage Scan

The main measuring series to identify the best voltage setup for the TRD were, in respect to the energy solution, executed before the clusterizing tool update. This means that the compared old signal peak and wrong clusterized data might alter the energy solution per voltage setting. This does not concern the drift voltage of 500 V which is set to compromise between strong electrical field without noise avalanche production (see **2.3.1**), but the anode voltage setting. These measurements were not repeated due to low assumed effect and lack of time.

SPADIC 1.1

The next SPADIC generation, SPADIC 1.1 is likely to be soon released. This thesis results (especially concerning TRD and readout problems) contributed to discover bugs of the old SPADIC 1.0 which have to be resolved for the new SPADIC 1.1.
A repetition of the measurements with similar parameters and the new SPADIC 1.1 should allow more accurate measurement due to e.g. the fixed sign-recognition problem that would enable measurements with two different trigger thresholds. This would lead to a considerably more precise discrimination between signals and noise and therefore better energy solution.

6.9 Final Conclusion

The major goal to provide the first experimental setup for detector data acquisition and a signal readout recognizable as a Fe-55 energy spectrum was accomplished. Setup parameters were set and the larger problems that could not be solved were recognized. Although the final energy resolution is not good enough for a final experimental use, it offers a comparison to other detector types with similar setups.

Appendix A

Uncertainties

$$\Delta\alpha = \frac{\Delta x \cdot \sqrt{((d_c - d_s)^2 + 8b^2)}}{(d_c - d_s)^2 + 4b^2} = 0.0036\,\text{rad} \tag{A.1}$$

$$A(\text{July 2015}) = A(\text{May 2006}) \cdot e^{-ln(2)\frac{t}{t_H}} = 3.63\,\text{MBq} \tag{A.2}$$

With activity A of the source and sources half-life $t_H = 2.737\,\text{y}$ [10]. Informations on sources initial activity of 37 MBq were ordering documents of the Institut für Kernphysik Münster.

Table A.1: Final energy resolution fit function errors and set energy resolution

$\Delta A_{K\beta}$	5.01 eV
$\Delta\sigma_{K\beta}$	54.32 eV
ΔA_2	22.91 eV

$$\Delta(\Delta E) = \sqrt{\left(\frac{\Delta\sigma_1}{E_1}\right)^2} \tag{A.3}$$

$$P(\text{multi hit}) = 1 - (P(\text{one hit}) + P(\text{no hit})) = 1 - (1 + \mu) \cdot (e^{-\mu}) \tag{A.4}$$

With

$$\mu = \frac{t_{message}}{t_{Fe55}} \tag{A.5}$$

Computed with the Poisson distribution with duration $t_{message} = 1.82848\,\mu\text{s}$ of one message and average time $t_{Fe55} = 122.841\,\mu\text{s}$ between two photon hits at one readout channel.

Appendix B

Pictures

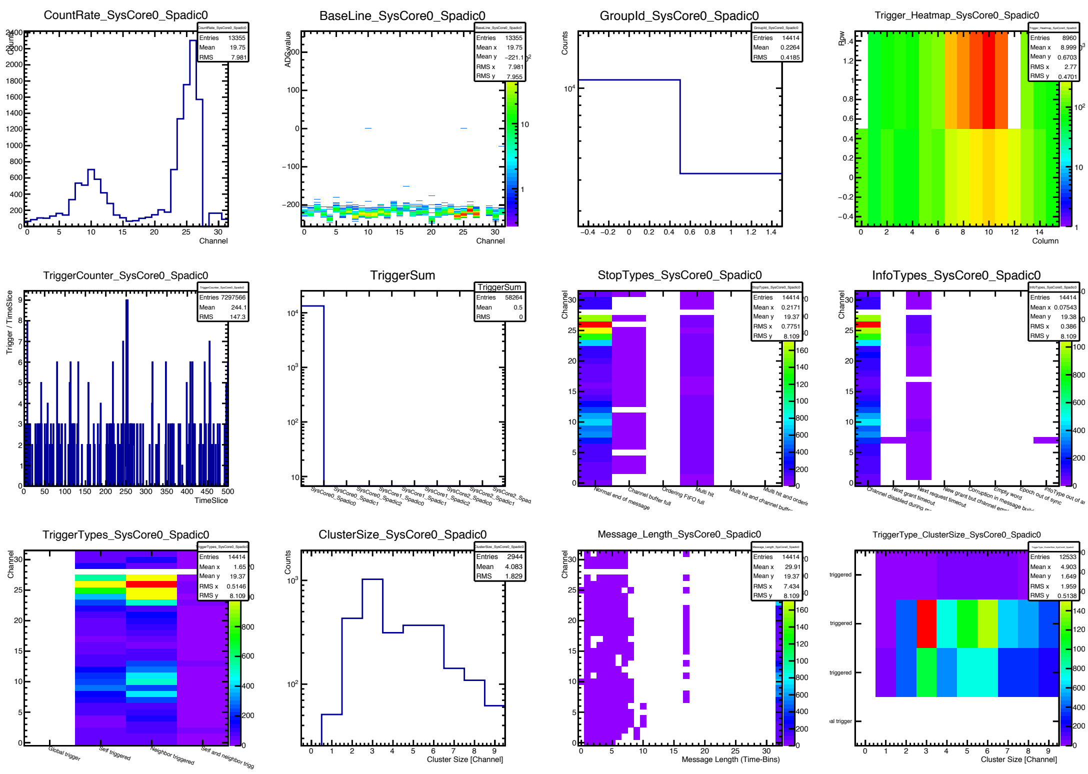

FIGURE B.1: Exemplary control histogram monitor for a run with differential thresholds 20/20 at final settings

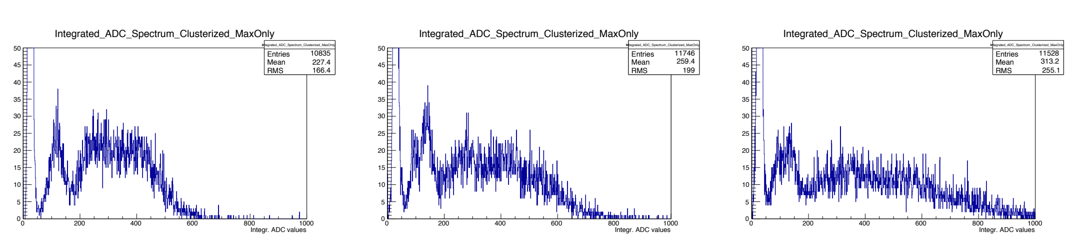

FIGURE B.2: Exemplary comparison of ADC Integrated spectrum at different anode voltages: 1700 V (left), 1750 V (middle) and 1850 V (right)

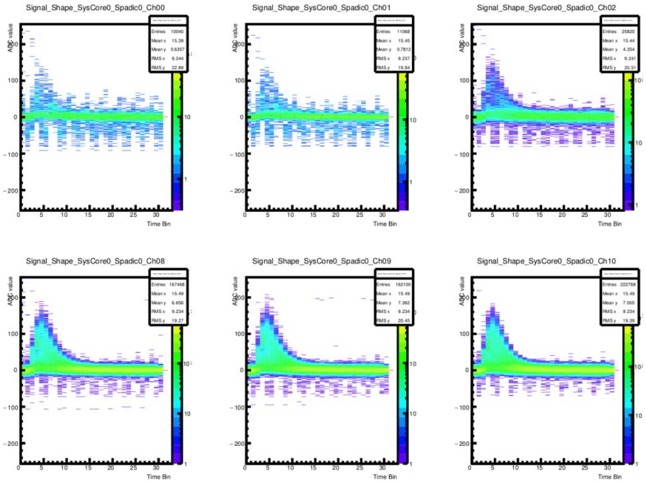

FIGURE B.3: Signal Shape at absolute thresholds -250/-170 with direct SPADIC grounding

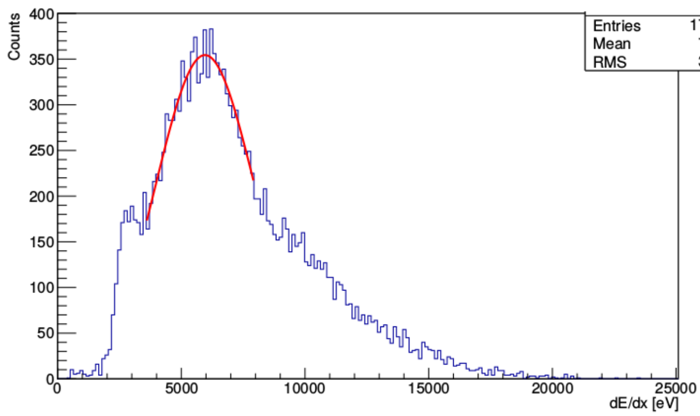

FIGURE B.4: Final filtered Integrated ADC spectrum measured at absolute thresholds -170/-170 with applied gauss-fit for Kβ peaks

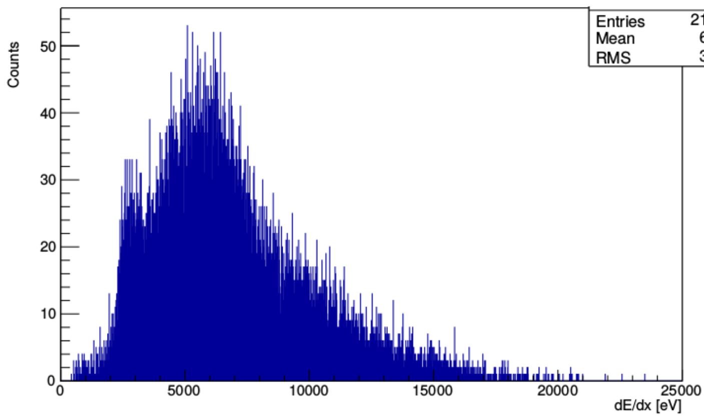

FIGURE B.5: Final filtered Integrated ADC spectrum measured at absolute thresholds -170/-170 unbinned

Bibliography

[1] The SPADIC project website. July 2015. URL http://www.spadic.uni-hd.de.

[2] CBM official homepage. June 2015. URL http://www.fair-center.eu/for-users/experiments/cbm/introduction.html.

[3] Tomás Balog. Overview of the CBM detector system. *Journal of Physics: Conference Series*, 503(01201), 2014.

[4] P. Bandyopadhyay and C.U. Segre. Mucal on the web. September 2015. URL http://www.csrri.iit.edu/mucal.html.

[5] C. Bergmann. Development and test of a Transition Radiation Detector prototype for CBM @ FAIR(diploma thesis). 2009.

[6] C. Bergmann. Development and test of a Transition Radiation Detector prototype for CBM @ FAIR (phd thesis). 2014.

[7] R. Brun and F. Rademaker (editors). ROOT - an object oriented data analysis framework. *Nucl. Inst. Meth. in Phys. Res.*, 389:81–86, September 1997.

[8] J. de Cuveland. July 2015. URL https://github.com/cbm-fles/flesnet.

[9] E.P. Akishina, T.P. Akishina, V.V.Ivanov, A.I.Maevskaya, O.Yu. Denisova. Electron/pion identification in the CBM TRD applying a ω_n^k goodness-of-fit criterion. *Physics of Particles and Nuclei Letters*, 5(2):116–126, March 2008.

[10] M.-M. B, V. Chist, C. Duliieu, E. Browne, V. Chechev, N. Kuzmenko, R. Helmer, A. Nichols, E. Schnfeld, R. Dersch. Table de radionuclides. 3:5, 2004.

[11] C. Bergmann et al. Test of Münster CBM-TRD real-size detector and radiator prototypes at the CERN PS/T9 beam line. *CBM Progress Report*, page 78, January 2014.

[12] T. Armbruster et al. SPADIC - self-triggered charge pulse processing ASIC. *TPC Workshop presentation*, 2013. URL http://spadic.uni-hd.de/publications/talks/2013/02_02.pdf.

[13] A. Arend for the CBM TRD group. Status and first results of the CBM TRD prototype development. *Journal of Physics: Conference Series*, 426(1):1–20, January 1991.

[14] V. Friese. Simulation and reconstruction of free streaming data in CBM. *Journal of Physics*, 331, 2011.

[15] M. Kohn. Studies on a di-electron trigger for upsilon-mesons with the ALICE TRD. April 2014.

[16] J. M.Heuser, M.Deveau, C. Müntz and J. Stroth for the CBM Collaboration. Requirements for the silicon tracking system of CBM at FAIR. 2005.

[17] FAIR official homepage. June 2015. URL http://www.fair-center.eu.

[18] J. Randrup and J. Cleymans. *Physical Review*, 74(047901):611–612, 2006.

[19] W. Blum, W. Riegler, L. Rolandi. Particle detection with drift chambers. (2), 2008.

[20] A. Saba. ALICE experiment homepage. September 2015. URL http://aliceinfo.cern.ch/Public/en/Chapter2/Chap2_TRD.html.

[21] S. Sarkar, H. Satz, B. Sinha. The physics of the quark-gluon plasma. 2, 2010.

[22] K. Thomas. Auger electron spectroscopy (AES). August 2015. URL http://utep.edu/display/~ksthomas2/AES.

[23] D. Vernekohl. Small animal positron emission tomography with gas detectors. pages 87–88, April 2014.

Acknowledgements

Firstly I want to thank the members of my work group and Prof. Dr. Johannes P. Wessels for the possibility to work in his department.
Special thanks is due to my supervisors Martin Kohn and Dr. Cyrano Bergmann for their support at all stages of the work and Philipp Kähler for his aid and thesis review. The stressful final stage of my thesis was relieved by my office mate Felix Fidorra who offered help or distraction whenever needed.

Finally, I want to thank those who have shared and enriched my life for a long time:
My family, Lena, Raphael, Jojo and Carla and my favorite Münsteraner Nora, Helena, Eva and Jeremias.

Plagiatserklärung

Hiermit versichere ich, dass die vorliegende Arbeit **Characteristics of a CBM TRD** selbstständig verfasst worden ist, dass keine anderen Quellen und Hilfsmittel als die angegebenen benutzt worden sind und dass die Stellen der Arbeit, die anderen Werken auch elektronischen Medien dem Wortlaut oder Sinn nach entnommen wurden, auf jeden Fall unter Angabe der Quelle als Entlehnung kenntlich gemacht worden sind.

____

(Datum, Unterschrift)

Ich erkläre mich mit einem Abgleich der Arbeit mit anderen Texten zwecks Auffindung von Übereinstimmungen sowie mit einer zu diesem Zweck vorzunehmenden Speicherung der Arbeit in eine Datenbank einverstanden.

____

(Datum, Unterschrift)